Atmospheric Pollution Research 16 (2025) 102419

Contents lists available at ScienceDirect

Atmospheric Pollution Research

journal homepage: www.elsevier.com/locate/apr

Inverse modeling of 137Cs during Chernobyl 2020 wildfires without the first guess

Ondřej Tichý [a,c,*], Nikolaos Evangeliou [b], Anna Selivanova [c,d], Václav Šmídl [a]

[a] Institute of Information Theory and Automation, Czech Academy of Sciences, Prague, Czech Republic
[b] NILU, Department for Atmospheric & Climate Research (ATMOS), Kjeller, Norway
[c] National Radiation Protection Institute, Prague, Czech Republic
[d] Czech University of Life Sciences Prague, Prague, Czechia

ARTICLE INFO

Keywords:
Chernobyl wildfires
Inverse modeling
Plume bias correction
Multi-species emissions
JRODOS

ABSTRACT

This study estimates 137Cs emissions from Chernobyl wildfires in April 2020 using inverse modeling. Emissions are resolved with daily resolution by particle sizes (0.4 μm, 8 μm, 16 μm) and altitudes (up to 3 km). The inverse problem's complexity requires regularization due to its ill-posed nature. One potential way to regularize the problem is the use of the so-called first guess, i.e. emission taken from expert knowledge or previous literature. However, inappropriately chosen first guess may lead to serious bias in results or its availability may be limited for rapid response. We rather follow a Bayesian approach where all model parameters are considered as variables to be estimated from available data. We aim to combine three key principles: modeling of sparsity and smoothness of the emission vector, modeling of bounded ratios between released particle size/altitude fractions, and bias correction of the atmospheric transport model. All these principles proved their significance separately, however, we combine them in one comprehensive method to estimate the 137Cs emissions from the Chernobyl wildfires. The total released activity was estimated to be 458 GBq with uncertainty estimated to be 69 GBq. Our estimates also suggest that most of the activity has been released below a one-kilometer altitude with the more dominant role towards the smallest particle fraction than was considered in other studies. Using our estimate, we calculate the time-integrated volumetric activities of 137Cs over the domain using the JRODOS system and our findings well agrees with previous results.

1. Introduction

Estimation of an unknown release is a key step for the evaluation of accidental releases of hazardous material into the atmosphere. Particularly important are releases of radioactive materials, especially after Chernobyl and Fukushima Daiichi nuclear accidents (Evangeliou et al., 2017; Li et al., 2019). The typical approach is to use available information, such as satellite data or ambient measurements, and optimize the mismatch between a theoretical output and observations. However, further assumptions are often needed due to many uncertainties associated with a particular problem. In the case of wildfires, particle size fractions or altitude release distribution are particularly difficult to estimate (Kovalets et al., 2022). The first guess is often successfully used when available with associated uncertainties; however, it is also a source of possible bias in the calculations when limited information are available. Therefore, we propose to use a different form of regularization designed for complex multi-species scenarios such as wildfires, where restricted ratios between species and bias correction of an atmospheric model are used. We demonstrate the approach in the case of wildfires around Chernobyl in 2020.

During April 2020, the largest wildfires inside the exclusion zone were observed Talerko et al. (2021a) since the Chernobyl disaster, after other significant wildfires fires occurred in the past. In the case of the April 2020 wildfires, the first were reported on 3 April and lasted until 14 April when they were lowered by a cold front, rain, and the work of firefighters. Wildfires, however, started again on 16 April and were accompanied by a dust storm that occurred between 16 and 17 April (Kovalets et al., 2022). Approximately after 21 April, the wildfires became negligible and under the control of the authorities. The burned area in the exclusion zone has been estimated to be more than 80,000 ha while also the area outside the zone has been affected (Talerko et al., 2021a; Protsak et al., 2020). Therefore, wildfires cause radioactive emissions of a number of radionuclides from the soil and vegetation (Evangeliou and Eckhardt, 2020), including 137Cs which is one of the most important due to its relatively long half-live, more than 30 years.

* Corresponding author at: Institute of Information Theory and Automation, Czech Academy of Sciences, Prague, Czech Republic.
E-mail address: otichy@utia.cas.cz (O. Tichý).

https://doi.org/10.1016/j.apr.2025.102419
Received 19 September 2024; Received in revised form 13 January 2025; Accepted 14 January 2025
Available online 7 February 2025
1309-1042/© 2025 Turkish National Committee for Air Pollution Research and Control. Production and hosting by Elsevier B.V. All rights are reserved, including those for text and data mining, AI training, and similar technologies.

Table 1
Comparison of relevant approaches for the Chernobyl wildfires case in April 2020.

	Approach	Size fractions [μm]	Altitudes [m]	Estimate [GBq]	Uncertainty [GBq]
Evangeliou and Eckhardt (2020)	bottom-up	0.25, 8, and 16; fixed to 20, 20, 60%	taken from CAMS GFAS[c]	341	[46; 709]
Protsak et al. (2020)	bottom-up	–	–	690	–
Talerko et al. (2021a)	bottom-up	fixed to 1	fixed between 0–200	574	–
Baró et al. (2021)	top-down	0.17, 1.1, and 3	0–3000 and 1000–3000	600[a]	[400; 800]
De Meutter et al. (2021)	top-down	N/A	fixed to 500	650	[220; 1810]
Masson et al. (2021)	top-down	modeled using fixed deposition velocity	fixed between 0–500	950	[700; 1200]
Kovalets et al. (2022)	combined	0.25, 8, and 16; tested values [10 20]%, [0 20]%, and the rest	taken from CAMS GFAS[c]; tested distribution	448+21[b]	[39 1530] and [3 93][b]
our study	top-down	0.4, 8, and 16; estimated distribution	0-3000; estimated distribution	458	[389; 527]

[a] Only for the period 4 to 13 April.
[b] Separately from wildfires fires and dust storm.
[c] (Kaiser et al., 2012).

The emissions of 137Cs and associated consequences are of great scientific as well as public interest. However, the assessment of wildfires highly depends on the knowledge of the emissions, its particle fractions composition, and altitude levels of smoke, which are information not easy to estimate or measure. There are two main approaches for emissions estimation, the bottom-up and top-down approaches (Nisbet and Weiss, 2010). In the case of wildfires, the bottom-up approach is based on knowledge of vegetation and soil contamination and on the assumption of a factor of radioactivity being resuspended to the atmosphere, while the top-down approach is based on analysis of ambient concentration measurements combined with the theoretical output from an atmospheric transport model. The bottom-up approach was used at an early stage for the case of the Chernobyl wildfires (Protsak et al., 2020; Evangeliou and Eckhardt, 2020; Talerko et al., 2021a) using information from Fire Information for Resource Management System (FIRMS) provided by NASA satellites. Later, estimates using top-down approaches from ambient concentration measurements appeared for part of the period (Baró et al., 2021) or the whole wildfire period (De Meutter et al., 2021; Masson et al., 2021). A combination of these two approaches has been used by Kovalets et al. (2022) where spatial distribution and the first guess have been assumed based on satellite data and then used by an inversion algorithm. Details on used approaches, assumptions, and resulting estimates are given in Table 1. Table 1 demonstrates differences in key wildfire parameters, size fractions of released particles and their vertical distribution, respectively. Here, it is shown that most of the studies rely on fixed-size fractions of 137Cs releases or fixed ratio between multiple fractions based on laboratory findings (Hao et al., 2018). A similar method was performed for altitude levels of the releases where, typically, releases from a particular altitude range is considered. To avoid such assumptions, multiple particle size fractions and multiple release altitudes can be modeled using an atmospheric transport model. However, the inversion then becomes much more demanding since the releases are the result of the number of time-steps times the number of size fractions times the number of considered altitude levels. In that case, the inversion of unknown releases is much more demanding and further regularization is crucial for a meaningful solution.

Today, researchers focus on the top-down approaches where the majority of methods are based on modeling the mismatch between measurements and model predictions using Gaussian (Eckhardt et al., 2008; Launay et al., 2024) or, more recently, log-normal distributions (Liu et al., 2017; Dumont Le Brazidec et al., 2021). For more complex scenarios, a *multi-species inversion* method may be beneficial with assumptions of ratios between species such as that of Saunier et al. (2013), Katata et al. (2012) for the Fukushima emissions, by Zhang et al. (2017) for the sequential multi-nuclide source term estimation, or by Tichý et al. (2018) within a Bayesian inverse model relaxing strict ratios using a probabilistic model. To consider ratios within multi-species emissions is highly relevant for wildfires because there are different particle fractions as well as different emission altitudes which are most likely correlated.

The majority of methods modeling the mismatch between measurements and predictions, however, do not address the *bias* caused by inaccurate atmospheric modeling. There were attempts to directly correct some of atmospheric transport coefficients or weather reanalysis parameters (Bocquet, 2012; Mao et al., 2021; Kovalets et al., 2009) which, however, aim to correct only a part of a hypothetical bias. A general bias in atmospheric modeling has been corrected by the use of an ensemble (Crawford et al., 2022), when possible. Recently, there have been attempts to correct bias in atmospheric modeling formulated as a correction of the source-receptor-sensitivity (SRS) matrix within the minimization procedure (Li et al., 2018; Fang et al., 2021) where a preconditioning of the SRS matrix is used based on the spatial distance between every pair of measurements and calculated autocorrelation scale. The method has been later improved by emission rate oscillation-free regularization (Fang et al., 2022) which is relevant for long-distance modeling as well as for complex building scenarios (Dong et al., 2024). The complex information on the measuring network topology has been used for a bias correction model by Tichý et al. (2022) where the key assumption is that corrections of neighboring measurements are correlated preventing overparametrization.

In this paper, we combine the benefits of these two approaches, namely the multi-species inversion and the bias correction, in one inversion scheme to estimate the 137Cs emissions released during wildfires around Chernobyl in April 2020. Each specie is specified by its particle size fraction and altitude level. Similarly to Evangeliou and Eckhardt (2020) or to Kovalets et al. (2022), we assume 3 different particle fractions with mean diameters 0.4 μm, 8 μm, and 16 μm, respectively. However, we do not restrict the solution to given ratios assumed for the whole period as in Evangeliou and Eckhardt (2020) or a discrete hypothesis on ratios as in Kovalets et al. (2022). We assume 7 altitude levels of the 137Cs emissions ranging from 0 to 3000 meters since even 3000 meters level may be relevant for wildfires (Savenets et al., 2024) on a continental modeling scale. Rather than a setting of fixed ratios between these 21 combinations for each day of April 2020, we use wide intervals regularizing ratios between species (Tichý et al., 2018), letting the model fit measurements within these intervals. For the bias correction, we follow the model of Tichý et al. (2022) and we use the knowledge of measuring network topology to calculate the bias correlation of each SRS coefficient. We apply the method to the dataset

with 137Cs concentration measurements taken from Masson et al. (2021) with the use of the atmospheric transport model FLEXPART 10.4 (Pisso et al., 2019). The estimated emissions are then used in the JRODOS system to calculate time-integrated volumetric activities of 137Cs and to compare them to findings by Talerko et al. (2021a).

2. Case description, data, and atmospheric transport modeling

2.1. State of the art on Chernobyl fires

We shortly review the current state of the art regarding the Chernobyl wildfires in 2020. Evangeliou and Eckhardt (2020) used a bottom-up approach to estimate the total released activity at nearly 400 GBq across multiple radionuclides, with 341 GBq attributed specifically to 137Cs. Protsak et al. (2020) estimated 137Cs emissions to be 690 GBq which was later updated by Talerko et al. (2021a) to 574 GBq based on detailed analysis of Chernobyl exclusion zone landcover and fire locations using Fire Information for Resource Management System provided by NASA. A top-down approach was used by Baró et al. (2021) constraining the disproportion between measurements and the FLEXPART output using Bayesian methodology obtaining 137Cs emissions in the order of 600 GBq with uncertainty of 200 GBq for the period 4 to 13 April. De Meutter et al. (2021) analyzed the case using the Bayesian source reconstruction tool proposed in De Meutter and Hoffman (2020) also using FLEXPART dealing, notably, also with non-detections with a posterior median of 650 GBq with the uncertainty interval from 220 to 1810 GBq. A comprehensive study of the April 2020 Chernobyl wildfires case was proposed by Masson et al. (2021) with, to our knowledge, the most complete 137Cs concentration measurement dataset. For inverse modeling, they used the Eulerian 1dx model within the C3X operational platform (Quélo et al., 2007) and the logarithmic model of residuals between measurements and model outputs (Saunier et al., 2019). The estimated total emission was between 700 to 1200 GBq with maximal activities estimated to be 362 GBq and 241 GBq for 16 and 19 April, respectively. An interesting combination of the bottom-up and the top-down approaches was proposed by Kovalets et al. (2022). Here, forty emission locations were identified together with three areas of emissions due to resuspension during the dust storm on 16 and 17 April. For these locations, several assumptions such as particles aerodynamic diameter, emission altitude distribution, or the first guess from work by Talerko et al. (2021a) were considered based on previous studies to construct the inverse problem. The estimated 137Cs emissions were 448 GBq from the wildfires, with uncertainty interval between 39 and 1530 GBq, and 21 GBq from the dust storm, with uncertainty interval between 3 and 93 GBq.

2.2. 137Cs measurements

There are numerous separated measurements of the Chernobyl 2020 wildfires such as from Ukraine (Protsak et al., 2020), IRSN, or IAEA. However, we use here the largest dataset from this event published by Masson et al. (2021). The dataset consists of more than thousand measurements from the first half of the year 2020 over Europe. From this dataset, we selected those measurements related to the April 2020 Chernobyl fires. We also consider only those measurements that are within the Chernobyl Exclusion Zone (CEZ) as was similarly done by Kovalets et al. (2022). This choice is motivated by the selected spatial discretization step, 0.5 degree, which is too coarse for short distance modeling. We end up with 792 relevant measurements used in this study. Note that there are large differences between measurements in measuring intervals (vary from 1 day to almost a month) and measured concentrations levels (from 0 to 700 μBqm^{-3}).

2.3. Atmospheric transport modeling in FLEXPART

To construct the SRSs, we use the Lagrangian particle dispersion model FLEXPART version 10.4 (Pisso et al., 2019) in the backward "retroplume" mode. The model releases computational particles that are tracked backward in time using hourly ERA5 (Hersbach et al., 2020) assimilated meteorological analyses from the European Center for Medium-Range Weather Forecasts (ECMWF) with 137 vertical layers and a horizontal resolution of $0.5° \times 0.5°$. FLEXPART simulates turbulence (Cassiani et al., 2015), unresolved mesoscale motions (Stohl et al., 2005) and convection (Forster et al., 2007). Particles are assumed to be spherical and influenced by gravitational settling, dry deposition, and in-cloud and below-cloud scavenging (Grythe et al., 2017). We tracked 137Cs particles 20 days backward in time for three different aerodynamic particle diameters (0.4 μm, 8 μm, 16 μm). The output resolution was set to $0.5°\times0.5°$ and the vertical resolution to seven layers (0–100, 100–500, 500–1000, 1000–1500, 1500–2000, 2000–2500, 2500–3000 m).

3. Standard inversion methodology with first guess

We adopted the concept of the source-receptor-sensitivity (SRS) matrix (Seibert and Frank, 2004) applied already in a number of atmospheric inverse modeling continental scenarios such as our case. Here, the relation between the potential point-source and a measurement, given by its coordinates and measurement time interval, is modeled as a sensitivity to a unit release by an atmospheric transport model. By doing this repetitively for each measurement and potential emission interval, we obtain the coefficient $m_{i,j}$ for each measurement i and each time-step j, forming a SRS matrix $\mathbf{M}$. Denoting the measurement vector as $\mathbf{y}$ and the emission vector $\mathbf{x}$, we can formulate the link between the measurements and reconstructions as

$$\mathbf{y} = \mathbf{M}\mathbf{x} + \mathbf{e}, \tag{1}$$

where the term $\mathbf{e}$ stands for model errors. The goal is to estimate unknown emission $\mathbf{x}$ from linear model (1). While it may seem like a simple problem, it is complicated for two essential properties of the SRS matrix $\mathbf{M}$:

1. ill-conditioned, the solution of (1) is not unique.
2. only an estimate of the true SRS matrix is available, due to uncertain weather fields. The observations are, in reality, generated by the model $\mathbf{y} = \mathbf{M}_{gt}\mathbf{x}_{gt}$, where subscript gt denotes ground truth of variable, hence the residue $\mathbf{e}$ also contains contributions from mismodelling $\mathbf{M} = \mathbf{M}_{gt} + \mathbf{\Delta}$.

These two fundamental issues need to be solved using some form of regularization of the inversion task. We now briefly review the first guess approach that is commonly used.

3.1. First guess

If the first guess of the source term $\mathbf{x}_0$ is available, it is advantageous to use it as a regularizer of Eq. (1), by defining the estimate as a minimizer of the loss function (Eckhardt et al., 2008; Tichý et al., 2020; Kovalets et al., 2022)

$$J(\mathbf{x}) = (\mathbf{y} - \mathbf{M}\mathbf{x})^T \mathbf{R}^{-1} (\mathbf{y} - \mathbf{M}\mathbf{x}) + \\ + \lambda (\mathbf{x} - \mathbf{x}_0)^T \mathbf{B}^{-1} (\mathbf{x} - \mathbf{x}_0), \tag{2}$$

where $\mathbf{R}$ is the covariance matrix stands for tolerance of deviation between measurement and model reconstruction and $\mathbf{B}$ is the covariance matrix which weights the penalization of proximity of the estimated emission from the first guess. We have intentionally introduced a scaling factor λ that scaled the regularization term for a given covariance matrix $\mathbf{B}$.

This regularization has essentially two tuning parameters:

$\mathbf{x}_0$ is the nominal value of the source term,

$\mathbf{B}$ the sensitivity matrix governing in which direction the estimate can deviate from the first guess.

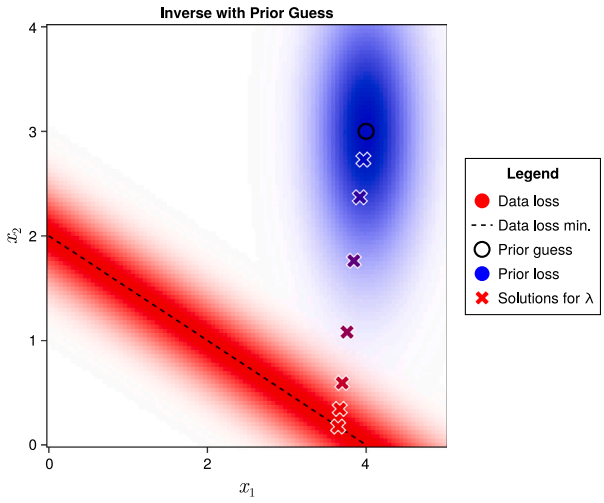

Fig. 1. Illustration of solutions of the toy inverse problem (3). The data loss is illustrated with a red color heatmap with a minimum denoted by the dashed line. The prior loss is illustrated in a blue heatmap with the first guess denoted by a circle. Solutions of the joint inverse problem for selected values of λ are displayed by crosses.

While selection of the first guess is often possible from other data, selection of the sensitivity matrix $\mathbf{B}$ is more challenging. It may be diagonal (Kovalets et al., 2022), or a weighted combination of diagonal and differential operator (Eckhardt et al., 2008).

3.2. Issues with the first guess

While the first guess approach is easy to understand, its consequences are not always obvious. Consider a trivial inverse problem with a single observation,

$$y = 1, \quad \mathbf{M} = [0.25, 0.5] \quad \mathbf{x}_0 = [4, 3], \quad \mathbf{R} = \mathbf{I}_2 \quad \mathbf{B} = \mathrm{diag}([0.5, 2]). \tag{3}$$

The solutions of this inverse problem for various choices of λ is displayed in Fig. 1. Note that the minimum of the data loss function (red color) is achieved on a line (i.e. the inverse has an infinite number of solutions) due to matrix $\mathbf{M}$ being ill-posed. Even a very small contribution from the regularization ($\lambda = 10^{-10}$) is sufficient to select one solution from this infinite set (red cross). With an increasing value of λ, the solution is approaching the first guess (circle) with the last (blue) cross of the joint solution displayed for $\lambda = 10^3$. The lower values of λ thus solve the fundamental problem of ill-posed $\mathbf{M}$,while higher values of λ are needed to divert the solution from the second fundamental problem of potentially incorrect solutions due to inaccurate estimate of $\mathbf{M}$.

This test experiment helps to clarify the severe sensitivity of the solution not only on the first guess $\mathbf{x}_0$ but perhaps more importantly on matrix $\mathbf{B}$. Note that solutions of the inverse problem for all values of λ lie on a line going through the first guess in the direction given by eigenvalues of $(\mathbf{M}^{\mathrm{T}}\mathbf{R}^{-1}\mathbf{M} + \lambda\mathbf{B}^{-1})$. While the first guess can often be obtained from other data, the choice of matrix $\mathbf{B}$ is often arbitrary.

3.3. Multi-dimensional source terms

These issues become much more apparent when the source term has multiple dimensions, such as those mentioned in Section 2.3 for the Chernobyl fires. In this case, the source term has 28 time steps with 3 size fractions that are being released at 7 altitude levels. Therefore, the inverse model has to consider that all of them contribute to the observations.

As an input data, we have 792 measurements forming vector $\mathbf{y} \in \mathbf{R}^{792}$. The SRS coefficients are calculated for 3 size fractions and 7 altitude levels, aiming to explain measurements using these 21 combinations, hence, the Eq. (1) can be reformulated as

$$\mathbf{y} = \sum_{\mathrm{f}=1\ldots3,\mathrm{a}=1\ldots7} \mathbf{M}_{\mathrm{f,a}}\mathbf{x}_{\mathrm{f,a}} + \mathbf{e}, \tag{4}$$

where f and a are indices of the fraction and altitude level, respectively. Model (4) can be rewritten into the standard form (1) by forming matrix $\mathbf{M} \in \mathbf{R}^{792\times(7*3*28)}$ by composing blocks of $\mathbf{M}_{\mathrm{f,a}}$ and corresponding $\mathbf{x}_{\mathrm{f,a}}$ into a single emission vector, $\mathbf{x} \in \mathbf{R}^{7*3*28}$. This results in even more ill-conditioned inverse problem which is motivation for further regularization. Note that design of the first guess, as well as matrix $\mathbf{B}$ becomes much more problematic.

The applicability of the first guess approach becomes complicated and alternative approaches are explored. Existing approaches use a very crude form of regularization, e.g. by splitting the vector of measurements $\mathbf{y}$ into contributions from size fraction: $\mathbf{y} = \sum_{\mathrm{f}=1}^{3} \mathbf{y}_{\mathrm{f}}$ and solving independent inversions (Evangeliou et al., 2017). In this paper, we seek more intuitive and fundamental alternatives.

4. Alternative regularizations in inverse modeling

Here, we describe alternative building blocks of our combined inverse methodology for multi-species inversion with bias correction. We use two elementary tools for regularization: (i) hard constraints that have physical meaning, and (ii) estimation of unknown hyperparameters (such as $\mathbf{B}$) from the data. Both of these tools violate the analytical solution of the least squares inversion and we need to find a numerical solution. Since we are interested also in the uncertainty of the source term estimation, we use the Bayesian interpretation of inversion.

4.1. Bayesian approach

In probabilistic interpretation, (2) has the meaning of negative logarithm of a joint model of data likelihood and prior:

$$p(\mathbf{y}|\mathbf{x}) = \mathcal{N}(\mathbf{Mx}, \mathbf{R}) \propto \exp\left(-\frac{1}{2}(\mathbf{y}-\mathbf{Mx})^T\mathbf{R}^{-1}(\mathbf{y}-\mathbf{Mx})\right), \tag{5}$$

$$p(\mathbf{x}) = \mathcal{N}(\boldsymbol{\mu}_{\mathbf{x}}, \mathbf{B}) \propto \exp\left(-\frac{1}{2}(\mathbf{x}-\boldsymbol{\mu}_{\mathbf{x}})^T\mathbf{B}^{-1}(\mathbf{x}-\boldsymbol{\mu}_{\mathbf{x}})\right), \tag{6}$$

where symbol $\propto$ denotes proportional equality (up to normalizing constant) and $\mathcal{N}$ denotes (multivariate) normal distribution with given mean and covariance. Considering the minimization of logarithm of this probabilistic model, the maximum aposteriori solution of (5)–(6) for $\boldsymbol{\mu}_{\mathbf{x}} = \mathbf{x}_0$ is exactly the same as the solution of minimization of (2). The key advantage of the Bayesian approach is that it allows extension of the model to unknown variables $\mathbf{R}$ and $\mathbf{B}$ such as that they can be estimated from the data. This is not possible with formulation (2) where matrices $\mathbf{R}$ and $\mathbf{B}$ need to be selected manually.

Estimation of the additional parameters $\boldsymbol{\theta}$, e.g. elements of $\mathbf{B}$, can be obtained using the variational Bayes methodology (Šmídl and Quinn, 2006) which approximates the posterior by conditionally independent factors satisfying conditions:

$$\tilde{p}(\mathbf{x}|\mathbf{y}) \propto \exp\left(\mathrm{E}_{\tilde{p}(\boldsymbol{\theta}|\mathbf{y})} \ln p(\mathbf{y}, \mathbf{x}, \boldsymbol{\theta})\right), \tag{7}$$

$$\tilde{p}(\boldsymbol{\theta}|\mathbf{y}) \propto \exp\left(\mathrm{E}_{\tilde{p}(\mathbf{x}|\mathbf{y})} \ln p(\mathbf{y}, \mathbf{x}, \boldsymbol{\theta})\right), \tag{8}$$

where $\mathrm{E}()$ denotes expected value of given argument. When more than one additional variable is considered, each new variable adds it approximate posterior analogically to (8).

The set of implicit Eqs. (7)–(8) is typically solved iteratively by a coordinate descent algorithm by sequentially updating the estimate of each variable. I.e. estimating $\tilde{p}(\mathbf{x})$ from (7) using previous estimate of $\tilde{p}(\boldsymbol{\theta})$, followed by estimating $\tilde{p}(\boldsymbol{\theta})$ using previous $\tilde{p}(\mathbf{x})$ until convergence. An advantageous property of this approach is that solution of

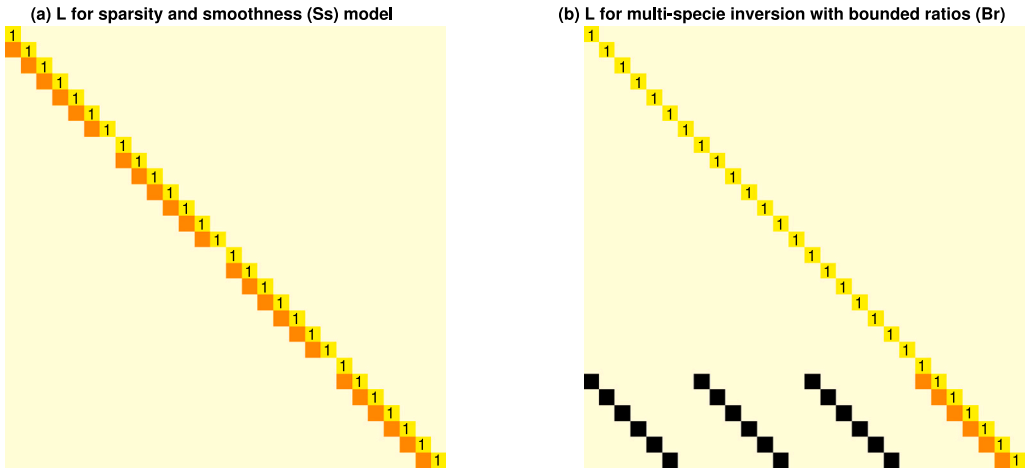

Fig. 2. The schemes of the matrix **L** implying the structure of the covariance matrix in the case of the sparsity and smoothness model (a) and the multi-species inversion with bounded ratios (b). All light yellow elements are zeros while yellow elements with '1' sign are ones. Orange elements denote variables of the sparsity and smoothness model and black elements denote variables of the multi-species inversion with bounded ratios model, respectively. Both are estimated within the variational Bayes procedure.

$\tilde{p}(\mathbf{x})$ is typically closely related to (2), giving the procedure a nice interpretation as automatic tuning of coefficients of the well known problem.

However, estimation of the full matrices **R** and **B** form the data is unrealistic since their number of parameters is much higher than the number of available data. Therefore, we need to make some modeling choices that are described next.

4.2. Sparsity and smoothness model (Ss)

The sparsity and smoothness prior model of the emission vector is based on a specific form of covariance matrix from the prior model (6), see full details and sensitivity study in Tichý et al. (2020). It is assumed that the covariance matrix **B**, since it is symmetric matrix, can be represented in a specific form of modified Cholesky decomposition, so that

$$\mathbf{B} = \mathbf{L}\mathbf{V}\mathbf{L}^T, \tag{9}$$

where $\mathbf{V} = \mathrm{diag}\,(\mathbf{v})$ is the diagonal matrix favoring a sparse solution and **L** is a lower bi-diagonal matrix with ones on its diagonal and unknown elements on its second lower diagonal, see the scheme in Fig. 2(a). Hence, the sub-diagonal vector **l** forming the matrix **L** stores correlation coefficients between neighboring elements of the emission vector **x**. The essence of the model is that by joint estimation of **v** and **l** from data, it preserves the sparse character of the emissions when there is evidence for sparsity in the data, while it favors the locally smooth character of emission when element **l** is estimated close to value -1.

For detailed derivation and estimation of posteriors of $\mathbf{x}, \mathbf{v}$, and **l**, we refer to Tichý et al. (2020).

4.3. Multi-species inversion with bounded ratios (Br)

For multi-species emissions, it may be beneficial to assume ratios between species within the emission vector **x**. In our case, species refer to 137Cs attached to 3 different particle sizes released at 7 different heights. Assuming m species forming the emission vector $\mathbf{x} = \left[\mathbf{x}_1^T, \ldots, \mathbf{x}_m^T\right]^T$ (in our particular case, $m = 21$), we will reformulate the model (9) to reflect ratios between one specific species, mth, and all the others (Tichý et al., 2018). These ratios can be then fixed when known, or bounded within the estimation procedure to a specific interval. In this paper, we bound these ratios between species elements (index t) as

$$x_{k,t} = r_{k,t} x_{m,t}, \quad a_{k,t} < r_{k,t} < b_{k,t}, \quad \forall k = 1, \ldots, m-1, \tag{10}$$

where $r_{k,t}$ is ratio between mth and kth element of **x** at tth time step. Boundaries **a** and **b** can be selected based on prior knowledge, however, since we have any in this case, we select them to $\mathbf{a} = 0.1$ and $\mathbf{b} = 10$ to obtain a reasonable range for each element. These boundaries can be transformed into the covariance matrix model (9), $\mathbf{B} = \mathbf{L}\mathbf{V}\mathbf{L}^T$, by modification of the matrix **L** as shown in the scheme in Fig. 2(b). By estimation of coefficients $r_{k,t}$ forming the matrix **L**, the model can, when evidence is present in data, prefer the ratio between the mth and all other species. Note that ratios set, e.g., to $[0.1; 10]$ do not imply that the final estimate of species in **x** will be exactly in this ratio since the model still has a degree of freedom in estimation of vector **v** which can shift results significantly. For the specific mth specie, we keep the Ss prior model as demonstrated in Fig. 2(b).

For detailed derivation and estimation of posteriors of $\mathbf{x}, \mathbf{v}$, and matrix **L**, we refer to Tichý et al. (2018).

4.4. Correction of the SRS matrix bias (Bc)

The bias correction method of the SRS matrix (Tichý et al., 2022) aims to address the second fundamental problem of inversion (Section 3), i.e. the inaccuracy of the SRS matrix **M**. The method uses additional information about the sensitivity of the SRS matrix around the sensor location both in terms of space and time. Specifically, we assume that the measured field $y_{i,j}$ at location s_h, s_v and time t may be incorrectly predicted by the SRS matrix because of inaccurate alignment of the location and time of the prediction. Therefore, we aim to estimate the correction terms in terms of spatial and temporal shifts of the SRS matrix using Taylor approximation:

$$\begin{aligned} \tilde{m}_{ij} &\approx m_{ij} + h_{h,i}\Delta_{h,i} + h_{v,i}\Delta_{v,i} + h_{t,i}\Delta_{t,i}, \\ \Delta_{h,i} &= \frac{m(s_{h,i} + \Delta s_h, s_{v,i}, t_i) - m(s_{h,i} - \Delta s_h, s_{v,i}, t_i)}{2\Delta s_h}, \end{aligned} \tag{11}$$

Rewriting (11) into matrix forms, the linear inverse problem is reformulated as

$$\mathbf{y} = \left(\mathbf{M} + \mathbf{H}_h\boldsymbol{\Delta}_h + \mathbf{H}_v\boldsymbol{\Delta}_v + \mathbf{H}_t\boldsymbol{\Delta}_t\right)\mathbf{x} + \mathbf{e}, \tag{12}$$

where **M** is the nominal SRS matrix, the $\boldsymbol{\Delta}_h$, $\boldsymbol{\Delta}_v$, and $\boldsymbol{\Delta}_t$, where horizontal, vertical, and temporal concentration shifts, respectively, calculated as gradients of the SRS in the given direction, see details in Tichý et al. (2022). The actual corrections $\mathbf{H}_h = \mathrm{diag}\,(\mathbf{h}_h)$, $\mathbf{H}_v = \mathrm{diag}\,(\mathbf{h}_v)$, and $\mathbf{H}_t = \mathrm{diag}\,(\mathbf{h}_t)$ are unknown diagonal weights (*bias corrections*) of each correction matrix. This reformulation leads to the bilinear inverse problem where both, corrected SRS matrix and the source term, respectively, need to be estimated.

Table 2
Summary of all combinations of the tested algorithms.

Sparsity and smoothness (Ss)	Bounded ratios with Ss (Br+Ss)	Bias correction with Ss (Bc+Ss)	Combined Bc+Br+Ss
input: $\mathbf{y}, \mathbf{M}$	input: $\mathbf{y}, \mathbf{M}$, $\mathbf{a}$, $\mathbf{b}$	input: $\mathbf{y}, \mathbf{M}, \boldsymbol{\Delta}_h, \boldsymbol{\Delta}_v, \boldsymbol{\Delta}_t, \mathcal{I}$	input: $\mathbf{y}, \mathbf{M}, \boldsymbol{\Delta}_h, \boldsymbol{\Delta}_v, \boldsymbol{\Delta}_t, \mathcal{I}$, $\mathbf{a}$, $\mathbf{b}$
iterate until convergence:	iterate until convergence:	iterate until convergence:	iterate until convergence:
► estimate $\mathbf{l}, \mathbf{v}$	► estimate $\mathbf{l}, \mathbf{v}$	► estimate $\mathbf{l}, \mathbf{v}$	► estimate $\mathbf{l}, \mathbf{v}$
	► estimate $\mathbf{r}$		► estimate $\mathbf{r}$
► estimate $\mathbf{x}$	► estimate $\mathbf{x}$	► estimate $\mathbf{x}$	► estimate $\mathbf{x}$
		► estimate $\mathbf{h}_h, \mathbf{h}_v, \mathbf{h}_t$	► estimate $\mathbf{h}_h, \mathbf{h}_v, \mathbf{h}_t$
output: $\mathbf{x}$	output: $\mathbf{x}$	output: $\mathbf{x}$, $\mathbf{h}_h, \mathbf{h}_v, \mathbf{h}_t$	output: $\mathbf{x}$, $\mathbf{h}_h, \mathbf{h}_v, \mathbf{h}_t$

The estimation problem would be over-parametrized by the introduction of bilinear model (12) unless further assumptions on bias corrections would not be imposed. Two key assumptions are considered by Tichý et al. (2022). First, each bias correction, i.e. elements of $\mathbf{h}_h$, $\mathbf{h}_v$, and $\mathbf{h}_t$, respectively, are bounded to a small fixed interval, typically $[-1; +1]$, to ensure that only small corrections are allowed in time and space. This choice implies the possible shift of one step in time and space. Second, the model assumes that the bias corrections of neighboring sensors are correlated with unknown correlation coefficients estimated using the model, with a predefined set of correlated sensors as the set $\mathcal{I}$.

For detailed derivation and estimation of posteriors of $\mathbf{h}_h$, $\mathbf{h}_v$, and $\mathbf{h}_t$, we refer to Tichý et al. (2022).

4.5. Multi-species inverse model with elastic plume bias correction

Thanks to the variational Bayes approximation, Eq. (7), methods for regularization introduced in Section 4 can be arbitrary combined, yielding methods with different assumptions, inputs, and different performance. Possible combinations are summarized in Table 2 with the input needed for the run, variables to be estimated, and the output of each algorithm.

Our goal is to combine bias correction with bounded ratios algorithm in one comprehensive methodology, however, we will provide also results for other combinations in an ablation study so that we study the performance and contributions of the regularization.

5. Application to Chernobyl ^{137}Cs dataset

First, we perform an ablation study to discuss the results of methods on the 137Cs Chernobyl fires 2020 dataset, Section 2.2, modeled using FLEXPART atmospheric transport model, Section 2.3. The purpose of the ablation study is to demonstrate that to use of all parts of the model together provides better results than to use them separately. Second, we study the results of the best method in detail and compare them with other literature estimates. Third, we use the best emission estimate as an input to the JRODOS atmospheric modeling system to perform an assessment of the 137Cs release to the environment, similarly as done, e.g., by Talerko et al. (2021a).

5.1. Best model selection

We apply four model combinations presented in Table 2 to the 137Cs Chernobyl fires 2020 dataset. The results of all four methods are given in Fig. 3, top panel, where the results of the sparsity and smoothness (Ss) model are given using green bars, the results of the method with bounded ratios (Ss+Br) are given using magenta bars, the results of bias correction with sparsity and smoothness model (Bc+Ss) are given using light blue bars, and the results of bias correction with bounded ratios method (Bc+Ss+Br) are given using blue bars. The total estimated emissions are given in legend for each method. The results are accompanied by the scatter plots between measurements and reconstructions using the given methods in the bottom panels of Fig. 3 together with calculated correlation coefficients (r), normalized mean absolute error (nMAE), and the root mean squared logarithmic error (RMSLE), defined as

$$r = \frac{\sum_i \left(y_{i,\text{model}} - \overline{\mathbf{y}}_{\text{model}}\right)\left(y_i - \overline{\mathbf{y}}\right)}{\sqrt{\sum_i \left(y_{i,\text{model}} - \overline{\mathbf{y}}_{\text{model}}\right)^2}\sqrt{\sum_i \left(y_i - \overline{\mathbf{y}}\right)^2}} \tag{13}$$

$$\text{nMAE} = \frac{\sum_{i=1}^{p} |y_{i,\text{model}} - y_i|}{\sum_{i=1}^{p} y_i} \tag{14}$$

$$\text{RMSLE} = \sqrt{\frac{1}{p}\sum_{i=1}^{p}\left(\log y_{i,\text{model}} - \log y_i\right)^2} \tag{15}$$

where $y_{i,\text{model}}$ is reconstructed measurement by the selected model and $\overline{\mathbf{y}}$ denotes mean of the measurements or reconstructions, respectively. These values are provided in the title of each scatter plot n the bottom panels of Fig. 3. For all cases, it can be observed that the good fit was obtained for high values of measurements while there are some not well-fitted values of lower concentration measurements. This is probably caused by two factors. First, we approximate the wildfires as the point-source, however, the source is the case of Chernobyl wildfires spreads over few degrees in longitude which causes a bias in atmospheric modeling. Second, the measurements below 1 μBqm^{-3} are almost all from large distances, see Fig. 6. For this large distances, the dispersion model is probably biased out of the reach of our bias correction method where surroundings of 4 degrees was considered.

Although the character of estimated emissions is similar, there are particular differences which should be mentioned. The most notable difference can be seen between 16 and 18 April, where Bc+Ss+Br method provides lower values for 16 April than the other methods and higher for 17 and 18 April. Note also the 23 April, where the three methods, Ss, Br+Ss, and Bc+Br+Ss, respectively, estimate activity between 41 and 53 GBq while the Bc+Ss method estimates only negligible activity here. However, note that significant activity in 23 April has been estimated also by e.g. Masson et al. (2021) to over 60 GBq using the same dataset; therefore, we consider this results as acceptable. Overall, the best r, nMAE, and RMSLE values has been achieved by the combination Bc+Br+Ss. Therefore, this result will be considered as our best estimate and will be discussed in detail in the next section.

5.2. Estimated emissions

The complete results of the Bc+Br+Ss method are given in Fig. 4, where the estimated mean is given using the blue line and the uncertainty of the estimate is displayed as the gray area. Here, the uncertainty is considered as 2 standard deviations of the posterior estimate (95% confidence interval). The resulting estimate is in general agreement with the knowledge on the Chernobyl wildfires case as well as with the other estimates from the literature, see Fig. 5. Our time period started on 2 April when no wildfires were observed in the area, which corresponds well with our estimate being close to zero. Our posterior then increases up to 75 GBq (with uncertainty between approximately 34 and 116 GBq) on 10 April and then significantly drops close to 10 GBq on 14 and 15 April when the fires were restricted and almost extinguished thanks to firefighters and precipitation. However, on 16 April, the wildfires combined with a dust storm broke up again leading to a significant increase of 137Cs emissions, up to 78 GBq (with uncertainty between approximately 47 and 108 GBq) on 18 April. After 19 April, wildfires have receded with our estimate being around 5 GBq per day which is, again, consistent with other estimates in the

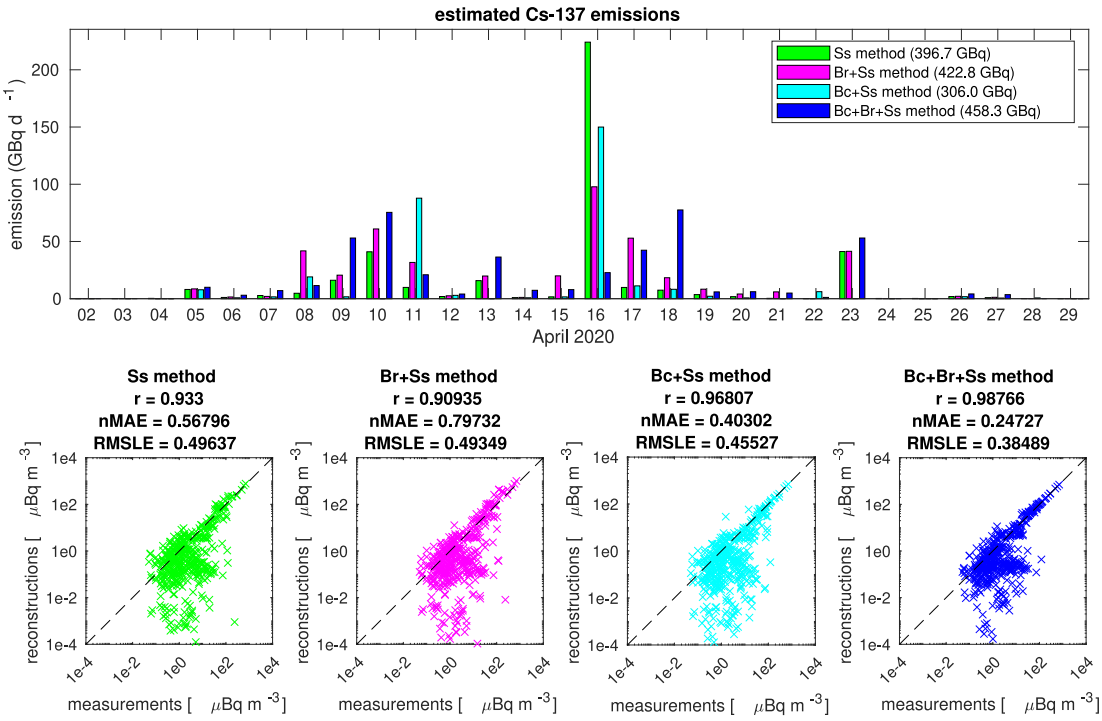

Fig. 3. Top: estimated 137Cs emissions from Chernobyl wildfires in April 2020 using all four tested combinations with the coloring given in the legend. Bottom: scatter plots between measurements and model reconstruction for all four tested combinations using the same coloring as in the top, associated with calculated r values.

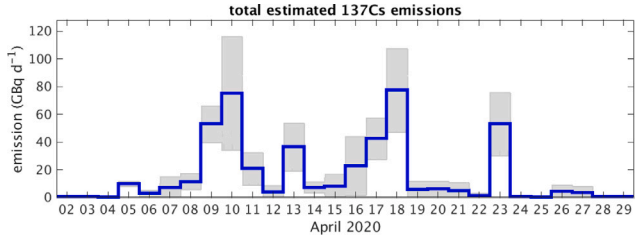

Fig. 4. The estimated 137Cs emissions from Chernobyl wildfires in April 2020 using selected Bc+Br+Ss method (full blue line) accompanied by the uncertainty bounds (fill gray regions) given as 2 standard deviations of the posterior estimate. In total, 458.3 +- 68.8 GBq of emitted 137Cs has been estimated.

literature, see Fig. 5. However, note that we have observed also an activity peak on 23 April with an estimated value of 53 GBq, although with a large uncertainty between 30 and 75 GBq. In the literature, most estimates ended on 20 or 22 April, however, the estimated activity after 20 April is in agreement with the calculations of De Meutter et al. (2021) or Masson et al. (2021), who observed a similar peak activity on 22 April (around 60 GBq). On the other hand, Kovalets et al. (2022) had no such result which may be caused by the strength of the first guess, since both, Masson et al. (2021) and Kovalets et al. (2022) respectively, used the same dataset but with different prior assumptions. After 23 April, the posterior activity was negligible with minor values on 26 and 27 April, however, with relatively large uncertainty. Our total estimated emission is 458.3 GBq with uncertainty bounds [389.5; 527.1] GBq, which is consistent with other estimates. Also note that the uncertainty bounds are calculated from Gaussian distribution as the squared sum of uncertainties for each source term element, $\sqrt{\sum_j \mathrm{std}_{\mathbf{x},j}}$, while summed element-wise maximal possible differences for 2 standard deviations is much higher, approximately hundreds of GBq. Notably, our estimate is obtained without any first guess available to the method.

The differences between our and other estimates, Fig. 5, may be caused by several reasons. Different techniques have been used, from analysis of satellite data and assumptions on released activity based on land-use to inverse modeling based on comparison of measurements and model output. The used atmospheric transport model driven with selected weather reanalysis is also source of differences, which can be also caused by different selection of transport model parameters. Another source of differences is assumed particle size fractions and considered altitude levels by other studies, see Table 1. We assume fine discretization of these parameters while the proportions of emissions are fully estimated from data.

The scatter plot between measurements and the reconstructions by the model is displayed in Fig. 6, with values below level 10^{-4} $\mu\mathrm{Bqm}^{-3}$ cropped for better visibility. Here, each data point has coloring according to its distance from the emission location, below 5, 10, 20, and up to 20 degree radius using blue, green, orange, and magenta colors, respectively. The correlation coefficient, defined in Eq. (13), estimated for our best model is $r = 0.98766$. Outliers in the scatter plot are studied in Fig. 7. Here, the outliers are displayed using red markers on the left panel, while total sensitivities for each day associated to outliers are displayed on the right panel. In this sense, days associated with the worst fit between measurements and reconstructions are 5, 14, 20, 21, and 22 April. However note that the estimated emissions for these days, Fig. 4, still well agree with general knowledge on this Chernobyl wildfires case. It can be seen that the best fit is reached for the largest measured values, which are, naturally, also the closest ones to the emission location. This is an expected behavior of the used model with quadratic loss combined with the bias correction method (Tichý et al., 2022) seeking for the best fit, with possible corrections from measurement spatiotemporal surroundings. The bias corrections for selected days 8 and 10 April are displayed in Fig. 8. Here, the lengths of lines denoting each correction are in the same scale as each map, while the green coloring denotes a positive shift in the time domain and the red coloring denotes a negative shift in the time domain, with the maximal shift set to one day. For both days, the behavior of the bias correction method is illustrated where corrections of measurements close to each other in the spatial domain are correlated. Prior values of correlations are set to zero, hence, only those that do not fit to the model are corrected.

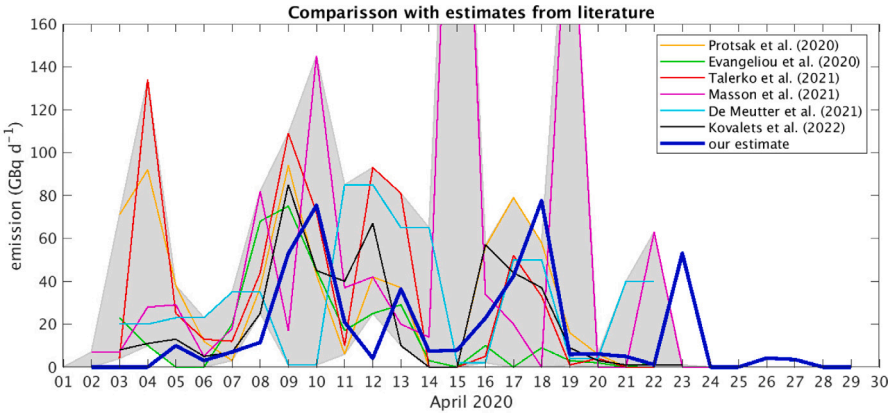

Fig. 5. Comparison between our estimate (thick blue line) and other estimates taken from literature (see coloring descriptions in legend). The gray region denotes the minimum and maximum of those from literature for each day.

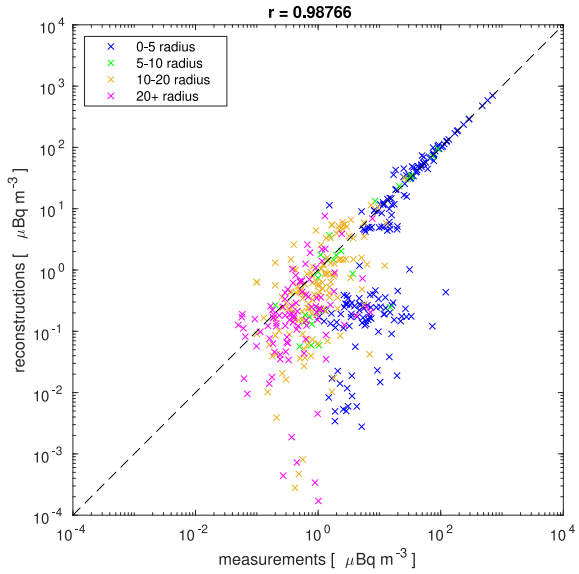

Fig. 6. The scatter plot between measurements and reconstruction by the model for the selected method. The coloring denotes the distance of each measurement from the source: between 0 and 5 degrees (blue), between 5 and 10 degrees (green), between 10 and 20 degrees (orange), and up to 20 degrees (magenta).

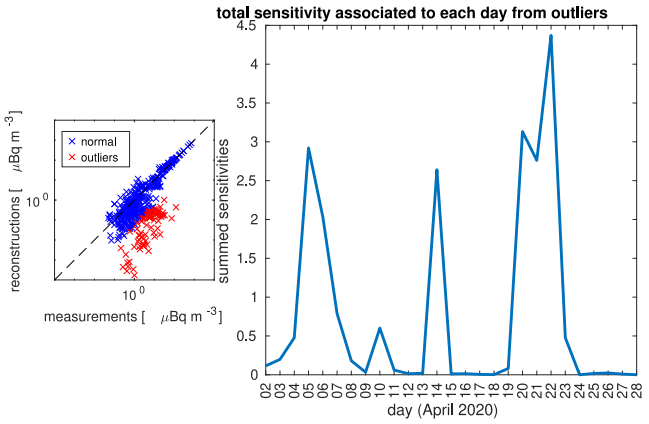

Fig. 7. Left: The same scatter plot as in Fig. 6 is displayed, here with red coloring of outliers of reconstructions. Right: total sensitivity for each day associated to outliers.

5.2.1. *Estimated fraction and altitude distributions*

The estimated distributions of activity from each particle fraction, 0.4 μm, 8 μm, and 16 μm, and each vertical level, 0–100, 100–500, 500–1000, 1000–1500, 1500–2000, 2000–2500, and 2500–3000 m, are given in Fig. 9 using different coloring, see legend for details. The estimated fraction distributions of released activity are 48%, 16%, and 36%, of 0.4 μm, 8 μm, and 16 μm fraction size, respectively. The distribution between fractions 0.4 μm and 16 μm differs from those considered by Evangeliou and Eckhardt (2020) where 0.25, 8, and 16 μm are assumed as 20%, 20%, and 60%, respectively. This result suggests that to consider released portion of 0.4 μm particles (or 0.25 μm as was taken in the literature case) of 20% as by Evangeliou and Eckhardt (2020) or 10% as in laboratory study by Hao et al. (2018) may be underestimated and higher values hypothesis may be considered within the inversion. Our calculations suggest that most of the activity, 53%, has been released below 1 kilometer altitude and only 14% has been released above 2 kilometers. However, note that these values and ratios are all estimated from the dataset combined with atmospheric transport model and bias imposed by model parametrization is possible. This may be significant specifically for large distances which are associated with lower concentration measurements, see Fig. 6, e.g. in Germany or France. To quantify this bias or uncertainties associated with estimated ratios are out of the scope of this paper and is potential subject for further research.

5.2.2. *Estimated parameters of dust storm*

Completely different characteristics of the emissions are estimated for the specific period of 16 and 17 April during the dust storm that occurred in the studied region (Talerko et al., 2021b). Here, 75% of the released activity has been estimated originating from the fraction 0.4 μm, leaving the rest 8% and 17% to 8 μm and 16 μm fraction size, respectively. This result is close to the estimate of Wagenbrenner et al. (2013) who reported that 1 μm particle emissions were 60% based on the territory previously hit by wildfire, rather than the assumption by Talerko et al. (2021b) who assumed this value as 40%. Interestingly, we have estimated that 99% of the activity for this period has been released below 1 kilometer altitude level, leaving the activity released above 1 kilometer negligible.

5.3. *JRODOS simulations*

In order to simulate wildfires in the Chernobyl exclusion zone, the JRODOS (Java-based Real-time Online DecisiOn Support) tool was utilized (RODOS team, 2019). The JRODOS was originally developed to forecast the atmospheric dispersion of radionuclide releases following nuclear accidents (Raskob et al., 2016). However, JRODOS contains a built-in module designed to simulate wildfires, using data on known

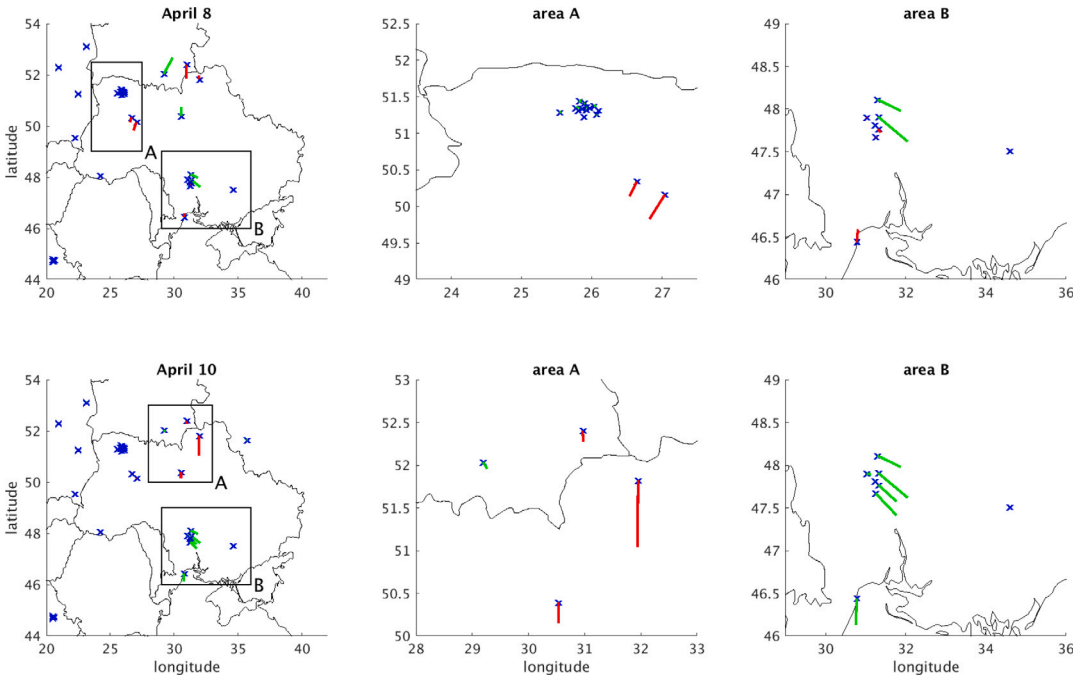

Fig. 8. The demonstration of the bias correction method applied to the Chernobyl wildfires dataset. Here, bias corrections for two selected days, April 8 and April 10, are given in the top and bottom panels, respectively. Area A and area B are displayed on the left panels with zoomed selected regions for better visibility. Here, the scale of corrections is given proportional to each map with positive (green) and negative (red) time shift estimated.

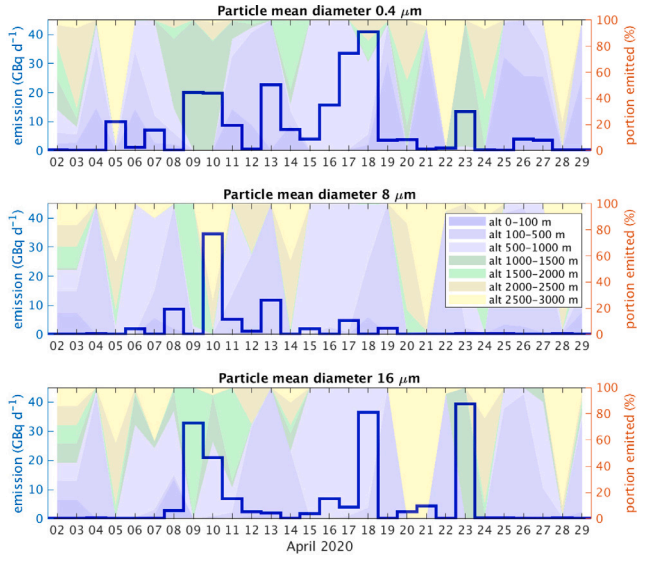

Fig. 9. The estimated 137Cs emissions with different particle fraction distribution of 0.4, 8, and 16 μm given in the top, middle, and bottom panel, respectively, using full blue lines with emissions amounts displayed in the left axis. The vertical emissions distribution for each particle fraction and each day is given using coloring areas, see the legend in the middle panel, where the bottom (below 1 kilometer) layers are displayed using blue filled regions, the middle (between 1 and 2 kilometers) layers are displayed using yellow filled regions, and the top (between 2 and 3 kilometers) are displayed using green filled regions, with percentage displayed in the right axis.

wildfire areas, fire intensities, and surface activities (Ievdin et al., 2019). Nonetheless, we adopted an alternative approach, assuming simple emissions of 137Cs only, rather than modeling burned areas.

The source term was located in the Chernobyl power plant, with variations in release heights, intensities, and particle sizes. The overall activity of 137Cs in the simulated releases was 458 GBq. In the JRODOS simulations, the model chain "Emergency" was employed in conjunction with the RIMPUFF model (Thykier-Nielsen et al., 1999), setting the calculation radius to 800 km. The simulated release was modeled from April 2, 2020, to April 30, 2020 (672 h). The total duration of the simulations was from April 2, 2020, to May 1, 2020 (696 h), including one additional day. For this period, we used historical meteorological data from the NOAA Operational Model Archive and Distribution System (NOMADS), with a spatial resolution of 0.5 degrees (Rutledge et al., 2003).

In the simulations, we utilized 21 source terms with varying release intensities, depending on emission height and particle diameter. We considered three mean diameters: 0.4 μm, 8 μm and 16 μm, which were changed in the JRODOS particle set-up (Andronopoulos et al., 2016). Thus, for each particle size, seven source terms were created corresponding to seven height intervals. Subsequently, for each particle size, 13 simulations were conducted, taking into account selected emission heights ranging from 10 m to 2550 m, according to the feasible extent of simulations (Ievdin et al., 2017; Selivanova et al., 2023). We generated 39 simulation tasks, which were submitted to JRODOS and launched automatically. For automation of the simulations, we used scripts in R programming language. Subsequently, all maps of time-integrated air concentrations of 137Cs were exported from JRODOS for further processing. For various heights within the same interval, the corresponding maps were generated by averaging values in each cell (up to 2500 m). For heights exceeding 2500 m (up to 3000 m), the simulation results were largely negligible, particularly for small particles with a mean diameter of 0.4 μm. Based on these simulation outcomes, time-integrated air concentrations were computed only for heights up to 2550 m. Consequently, the maps for all height levels and particle sizes were summed.

The resulting map of time-integrated volumetric activities of 137Cs is presented in Fig. 10, which can be directly compared with simulations by Talerko et al. (2021a). Compared to results by Talerko et al. (2021a), there are resembling patterns of volumetric activities in general, both for the total map and for the maps of separated fractions. The differences in the maps (our simulations and Talerko et al. (2021a), respectively) can be caused by different assumptions utilized in both

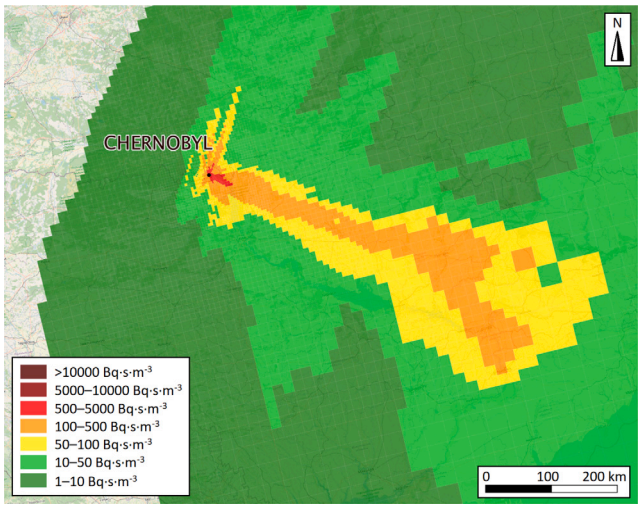

Fig. 10. Map of time-integrated volumetric ground level activities of 137Cs calculated using JRODOS driven with the estimated 137Cs emissions over the studied period (2 to 29 April 2020).

studies. While we simulate the point source emission with various emission altitudes (10 to 2550 m) and 3 different particle fractions (0.4 μm, 8 μm and 16 μm) using JRODOS driven with NOAA NOMADS meteorological data, Talerko et al. (2021a) employed LEDI atmospheric transport model driven with meteorological data from Ukrainian Hydrometeorological Center (UHMC) with runs from different burning areas, top altitude level at 200 meters and fixed particle size to 1 μm. The differences can be found also in the total released activity, 574 GBq and our estimate 458 GBq, and period considered, 17 days and our period 28 days. Nevertheless, both studies demonstrate similar results with slight variations, most likely due to different input parameters. The differences are probably caused by different vertical profile of emissions as well as by different size fraction composition of the source term.

6. Conclusions

We proposed the methodology for the inversion of multi-species emissions from 137Cs concentration measurements in the case of the Chernobyl wildfires in April 2020, where the emission consists of multiple particle fractions and multiple altitude levels. The assumption of bounded ratios between considered species and the use of bias correction of atmospheric transport model output allows us to suppress the need for the use of the first guess within the inversion. Our estimate in the case of the Chernobyl wildfires in 2020 agrees well with known information on the case regarding timing and the total released activity of 137Cs. We have estimated that 458 GBq of 137Cs has been released in total, with the correlation coefficient between measurements and model reconstructions being $r = 0.98766$. As a natural output of the method, we have estimated the particle size fraction and altitude levels distributions for each day, suggesting that the most of the activity has been released below 1 kilometer while during the dust storm on 16 and 17 April, almost all activity has been released below this altitude level. The fraction distribution has been estimated to be 48%, 16%, and 36%, of 0.4 μm, 8 μm, and 16 μm, respectively, which is in contrast to the assumption made often to 20%, 20%, and 60% in previous studies. This suggests that testing a higher percentage of particles lower than 1 μm during wildfires may be needed. We used the estimated 137Cs emission for further evaluation using the JRODOS system. The resulting concentration map agrees in general with previous findings based on the bottom-up approach.

CRediT authorship contribution statement

Ondřej Tichý: Writing – original draft, Visualization, Software, Methodology, Formal analysis, Data curation, Conceptualization. **Nikolaos Evangeliou:** Writing – review & editing, Software, Methodology, Conceptualization. **Anna Selivanova:** Writing – original draft, Software, Investigation. **Václav Šmídl:** Writing – original draft, Validation, Methodology, Investigation.

Declaration of competing interest

The authors declare that they have no known competing financial interests or personal relationships that could have appeared to influence the work reported in this paper.

Acknowledgments

This research has been supported by the Czech Science Foundation, grant no. GA24-10400S. FLEXPART model simulations are cross-atmospheric research infrastructure services provided by ATMO-ACCESS (EU grant agreement No 101008004). Nikolaos Evangeliou was funded by the same EU grant. The computations were performed on resources provided by Sigma2 - the National Infrastructure for High Performance Computing and Data Storage in Norway. Anna Selivanova has been supported by the project 2021B0003 of the Internal Grant Agency of the Faculty of Economics and Management, Czech University of Life Sciences, Prague.

Appendix A. Supplementary data

Supplementary material related to this article can be found online at https://doi.org/10.1016/j.apr.2025.102419.

Data availability

Data used in this study are available upon request.

References

Andronopoulos, S., Schichtel, T., Efthimiou, G., Bartzis, J., 2016. Updates of the atmospheric dispersion models inside the local scale model chain of RODOS regarding particles. Radioprotection 51, 101–103.

Baró, R., Maurer, C., Brioude, J., Arnold, D., Hirtl, M., 2021. The environmental effects of the april 2020 wildfires and the cs-137 re-suspension in the chernobyl exclusion zone: a multi-hazard threat. Atmosphere 12, 467.

Bocquet, M., 2012. Parameter-field estimation for atmospheric dispersion: application to the Chernobyl accident using 4D-Var. Q. J. R. Meteorol. Soc. 138, 664–681.

Cassiani, M., Stohl, A., Brioude, J., 2015. Lagrangian stochastic modelling of dispersion in the convective boundary layer with skewed turbulence conditions and a vertical density gradient: Formulation and implementation in the FLEXPART model. Bound.-Layer Meteorol. 154, 367–390.

Crawford, A., Chai, T., Wang, B., Ring, A., Stunder, B., Loughner, C.P., Pavolonis, M., Sieglaff, J., 2022. Evaluation and bias correction of probabilistic volcanic ash forecasts. Atmos. Chem. Phys. 22, 13967–13996.

De Meutter, P., Gueibe, C., Tomas, J., den Outer, P., Apituley, A., Bruggeman, M., Camps, J., Delcloo, A., Knetsch, G.J., Roobol, L., et al., 2021. The assessment of the April 2020 chernobyl wildfires and their impact on Cs-137 levels in Belgium and The Netherlands. J. Environ. Radioact. 237, 106688.

De Meutter, P., Hoffman, I., 2020. Bayesian source reconstruction of an anomalous Selenium-75 release at a nuclear research institute. J. Environ. Radioact. 218, 106225.

Dong, X., Zhuang, S., Xu, Y., Hu, H., Li, X., Fang, S., 2024. Multi-scenario validation of the robust inversion method with biased plume range and values. J. Environ. Radioact. 272, 107363.

Dumont Le Brazidec, J., Bocquet, M., Saunier, O., Roustan, Y., 2021. Quantification of uncertainties in the assessment of an atmospheric release source applied to the autumn 2017 106Ru event. Atmos. Chem. Phys. 21, 13247–13267. http://dx.doi.org/10.5194/acp-21-13247-2021.

Eckhardt, S., Prata, A., Seibert, P., Stebel, K., Stohl, A., 2008. Estimation of the vertical profile of sulfur dioxide injection into the atmosphere by a volcanic eruption using satellite column measurements and inverse transport modeling. Atmos. Chem. Phys. 8, 3881–3897.

Evangeliou, N., Eckhardt, S., 2020. Uncovering transport, deposition and impact of radionuclides released after the early spring 2020 wildfires in the Chernobyl exclusion zone. Sci. Rep. 10, 10655.

Evangeliou, N., Hamburger, T., Cozic, A., Balkanski, Y., Stohl, A., 2017. Inverse modeling of the Chernobyl source term using atmospheric concentration and deposition measurements. Atmos. Chem. Phys. 17, 8805–8824.

Fang, S., Dong, X., Zhuang, S., Tian, Z., Chai, T., Xu, Y., Zhao, Y., Sheng, L., Ye, X., Xiong, W., 2022. Oscillation-free source term inversion of atmospheric radionuclide releases with joint model bias corrections and non-smooth competing priors. J. Hazard. Mater. 440, 129806.

Fang, S., Zhuang, S., Li, X., Li, H., 2021. Automated release rate inversion and plume bias correction for atmospheric radionuclide leaks: A robust and general remediation to imperfect radionuclide transport modeling. Sci. Total Environ. 754, 142140. http://dx.doi.org/10.1016/j.scitotenv.2020.142140.

Forster, C., Stohl, A., Seibert, P., 2007. Parameterization of convective transport in a Lagrangian particle dispersion model and its evaluation. J. Appl. Meteorol. Climatol. 46, 403–422.

Grythe, H., Kristiansen, N., Zwaaftink, C., Eckhardt, S., Ström, J., Tunved, P., Krejci, R., Stohl, A., 2017. A new aerosol wet removal scheme for the lagrangian particle model flexpart. Geosci. Model Dev. 10, 1447–1466.

Hao, W., Baker, S., Lincoln, E., Hudson, S., Lee, S., Lemieux, P., 2018. Cesium emissions from laboratory fires. J. Air Waste Manage. Assoc. 68, 1211–1223.

Hersbach, H., Bell, B., Berrisford, P., Hirahara, S., Horányi, A., Muñoz-Sabater, J., Nicolas, J., Peubey, C., Radu, R., Schepers, D., et al., 2020. The ERA5 global reanalysis. Q. J. R. Meteorol. Soc. 146, 1999–2049.

Ievdin, I., Trybushnyi, D., Landman, C., 2017. JRodos Customization Guide Version 3.01.

Ievdin, I., Trybushnyi, D., Staudt, C., Landman, C., 2019. JRODOS User Guide.

Kaiser, J., Heil, A., Andreae, M., Benedetti, A., Chubarova, N., Jones, L., Morcrette, J.J., Razinger, M., Schultz, M., Suttie, M., et al., 2012. Biomass burning emissions estimated with a global fire assimilation system based on observed fire radiative power. Biogeosciences 9, 527–554.

Katata, G., Ota, M., Terada, H., Chino, M., Nagai, H., 2012. Atmospheric discharge and dispersion of radionuclides during the Fukushima Dai-ichi nuclear power plant accident. Part I: Source term estimation and local-scale atmospheric dispersion in early phase of the accident. J. Environ. Radioact. 109, 103–113.

Kovalets, I., Talerko, M., Synkevych, R., Koval, S., 2022. Estimation of cs-137 emissions during wildfires and dust storm in chernobyl exclusion zone in april 2020 using ensemble iterative source inversion method. Atmos. Environ. 288, 119305.

Kovalets, I., Tsiouri, V., Andronopoulos, S., Bartzis, J., 2009. Improvement of source and wind field input of atmospheric dispersion model by assimilation of concentration measurements: Method and applications in idealized settings. Appl. Math. Model. 33, 3511–3521.

Launay, E., Hergault, V., Bocquet, M., Dumont Le Brazidec, J., Roustan, Y., 2024. Bayesian inversion of emissions from large urban fire using in situ observations. Atmos. Environ. 120391.

Li, X., Li, H., Liu, Y., Xiong, W., Fang, S., 2018. Joint release rate estimation and measurement-by-measurement model correction for atmospheric radionuclide emission in nuclear accidents: An application to wind tunnel experiments. J. Hazard. Mater. 345, 48–62.

Li, X., Sun, S., Hu, X., Huang, H., Li, H., Morino, Y., Wang, S., Yang, X., Shi, J., Fang, S., 2019. Source inversion of both long-and short-lived radionuclide releases from the Fukushima Daiichi nuclear accident using on-site gamma dose rates. J. Hazard. Mater. 379, 120770.

Liu, Y., Haussaire, J.M., Bocquet, M., Roustan, Y., Saunier, O., Mathieu, A., 2017. Uncertainty quantification of pollutant source retrieval: comparison of Bayesian methods with application to the Chernobyl and Fukushima Daiichi accidental releases of radionuclides. Q. J. R. Meteorol. Soc. 143, 2886–2901.

Mao, S., Lang, J., Chen, T., Cheng, S., 2021. Improving source inversion performance of airborne pollutant emissions by modifying atmospheric dispersion scheme through sensitivity analysis combined with optimization model. Environ. Pollut. 284, 117186.

Masson, O., Romanenko, O., Saunier, O., Kirieiev, S., Protsak, V., Laptev, G., Voitsekhovych, O., Durand, V., Coppin, F., Steinhauser, G., et al., 2021. Europe-wide atmospheric radionuclide dispersion by unprecedented wildfires in the chernobyl exclusion zone, April 2020. Environ. Sci. Technol. 55, 13834–13848.

Nisbet, E., Weiss, R., 2010. Top-down versus bottom-up. Science 328, 1241–1243.

Pisso, I., Sollum, E., Grythe, H., Kristiansen, N.I., Cassiani, M., Eckhardt, S., Arnold, D., Morton, D., Thompson, R.L., Groot Zwaaftink, C.D., Evangeliou, N., Sodemann, H., Haimberger, L., Henne, S., Brunner, D., Burkhart, J.F., Fouilloux, A., Brioude, J., Philipp, A., Seibert, P., Stohl, A., 2019. The Lagrangian particle dispersion model FLEXPART version 10.4. Geosci. Model Dev. 12, 4955–4997. http://dx.doi.org/10.5194/gmd-12-4955-2019, URL: https://gmd.copernicus.org/articles/12/4955/2019/.

Protsak, V., Voitsekhovich, O., Laptev, G., 2020. Estimation of radioactive source term dynamics for atmospheric transport during wildfires in Chernobyl zone in Spring 2020. Ukr. Hydrometeorol. Inst. (in Ukrainian).

Quélo, D., Krysta, M., Bocquet, M., Isnard, O., Minier, Y., Sportisse, B., 2007. Validation of the polyphemus platform on the ETEX, Chernobyl and Algeciras cases. Atmos. Environ. 41, 5300–5315.

Raskob, W., Landman, C., Trybushnyi, D., 2016. Functions of decision support systems (JRodos as an example): overview and new features and products. Radioprotection 51, S9–S11.

RODOS team, 2019. Jrodos: Realtime online decision support system. https://resy5.ites.kit.edu/JRODOS/. (Accessed 22 May 2023).

Rutledge, G., Alpert, J., Stouffer, R., Lawrence, B., 2003. The NOAA operational model archive and distribution system (NOMADS). In: Realizing Teracomputing. World Scientific, pp. 106–129.

Saunier, O., Didier, D., Mathieu, A., Masson, O., Dumont Le Brazidec, J., 2019. Atmospheric modeling and source reconstruction of radioactive ruthenium from an undeclared major release in 2017. Proc. Natl. Acad. Sci. 116, 24991–25000.

Saunier, O., Mathieu, A., Didier, D., Tombette, M., Quélo, D., Winiarek, V., Bocquet, M., 2013. An inverse modeling method to assess the source term of the Fukushima nuclear power plant accident using gamma dose rate observations. Atmos. Chem. Phys. 13, 11403–11421.

Savenets, M., Rybchynska, V., Mahura, A., Nuterman, R., Baklanov, A., Kulmala, M., Petäjä, T., 2024. Seamless modeling of direct and indirect aerosol effects during April 2020 wildfire episode in Ukraine. Atmosphere 15, 550.

Seibert, P., Frank, A., 2004. Source-receptor matrix calculation with a Lagrangian particle dispersion model in backward mode. Atmos. Chem. Phys. 4, 51–63.

Selivanova, A., Hůlka, J., Kotík, L., Kuča, P., Rubovič, P., Malátová, I., Helebrant, J., Koc, J., Rulík, P., Vlček, O., 2023. Advanced simulation techniques for the transport of routine atmospheric discharges using the JRODOS system. Prog. Nucl. Energy 157, 104596.

Šmídl, V., Quinn, A., 2006. The Variational Bayes Method in Signal Processing. Springer.

Stohl, A., Forster, C., Frank, A., Seibert, P., Wotawa, G., 2005. Technical note: The Lagrangian particle dispersion model FLEXPART version 6.2. Atmos. Chem. Phys. 5, 2461–2474.

Talerko, M., Kovalets, I., Lev, T., Igarashi, Y., Romanenko, O., 2021a. Simulation study of radionuclide atmospheric transport after wildland fires in the Chernobyl exclusion zone in April 2020. At. Pollut. Res. 12, 193–204.

Talerko, M., Lev, T., Kashpur, V., 2021b. Estimation of the contribution of dust storm on April 16 2020to radioactive contamination of the atmosphere during forest fires in the Exclusion zone. Yad. Energetika Dovkyillya 8, 1–95 (in Ukranian).

Thykier-Nielsen, S., Deme, S., Mikkelsen, T., 1999. Description of the Atmospheric Dispersion Module RIMPUFF. Riso National Laboratory, PO Box 49.

Tichý, O., Šmídl, V., Evangeliou, N., 2022. Source term determination with elastic plume bias correction. J. Hazard. Mater. 425, 127776. http://dx.doi.org/10.1016/j.jhazmat.2021.127776.

Tichý, O., Šmídl, V., Hofman, R., Evangeliou, N., 2018. Source term estimation of multi-specie atmospheric release of radiation from gamma dose rates. Q. J. R. Meteorol. Soc. 144, 2781–2797. http://dx.doi.org/10.1002/qj.3403.

Tichý, O., Ulrych, L., Šmídl, V., Evangeliou, N., Stohl, A., 2020. On the tuning of atmospheric inverse methods: comparisons with the European Tracer Experiment (ETEX) and Chernobyl datasets using the atmospheric transport model FLEXPART. Geosci. Model Dev. 13, 5917–5934. http://dx.doi.org/10.5194/gmd-13-5917-2020.

Wagenbrenner, N., Germino, M., Lamb, B., Robichaud, P., Foltz, R., 2013. Wind erosion from a sagebrush steppe burned by wildfire: Measurements of PM10 and total horizontal sediment flux. Aeolian Res. 10, 25–36.

Zhang, X., Raskob, W., Landman, C., Trybushnyi, D., Li, Y., 2017. Sequential multi-nuclide emission rate estimation method based on gamma dose rate measurement for nuclear emergency management. J. Hazard. Mater. 325, 288–300.